Full vectorial feature of second-harmonic generation with full Poincaré beams

Li Zhang (张 莉)[1,2], Fei Lin (林 飞)[2], Xiaodong Qiu (邱晓东)[2], and Lixiang Chen (陈理想)[2,*]

[1]*School of Physics and Optoelectronic Engineering, Foshan University, Foshan 528000, China*
[2]*Department of Physics, Collaborative Innovation Center for Optoelectronic Semiconductors and Efficient Devices,
and Jiujiang Research Institute, Xiamen University, Xiamen 361005, China*
*Corresponding author: chenlx@xmu.edu.cn

We demonstrate the full vectorial feature of second-harmonic generation (SHG), i.e., from infrared full Poincaré beams to visible full Poincaré beams, based on two cascading type I phase-matching beta barium borate crystals of orthogonal optical axes. We visualize the structured features of the vectorial SHG wave by using Stokes polarimetry and show the interesting doubling effect of the polarization topological index, i.e., a low-order full Poincaré beam is converted to a high-order one. However, the polarization singularities of both C points and L lines are found to keep invariant during the SHG process. Our scheme could offer a deeper understanding on the interaction of vectorial light fields with media and can be generalized to other nonlinear optical effects.

OCIS codes: 190.2620, 260.6042.
doi: 10.3788/COL201917.091901.

Second harmonic generation (SHG), as the first nonlinear optical phenomenon observed in the experiment, can be traced back to the seminal work about frequency converting from 694.3 to 347.2 nm in crystalline quartz in 1961[1]. In the following year, Kleinman presented the electromagnetic theory of nonlinear dielectric polarization to explain the SHG phenomenon[2]. In 1968, Bloembergen *et al.* discovered the SHG effect on the semiconductor–air and metal–air interfaces[3]. As polarization-dependent SHG signals could provide useful information of the structural properties, SHG has become a standard spectroscopic tool to characterize materials[4]. Later, inspired by this attractive feature, Freund developed a kind of biological SHG imaging, i.e., SHG microscopy, to investigate the polarity of collagen fibers in rat tail tendons[5]. Since then, owing to no energy deposition to its interacted matters and localized excitation, SHG microscopy has been utilized for clinical imaging purposes to substantially reduce photobleaching and phototoxicity relative to fluorescence methods[6]. Nowadays, it has become a mature imaging technology and is widely used in biology and medicine fields[7]. Except for these applications in spectroscopy, the SHG process was also widely used for a high-power single-frequency fiber laser source[8], manipulation and generation of optical vortices[9], and optical image processing[10]. We note that all of the above works are almost focusing on the interaction of scalar light fields with nonlinear media.

Recently, vector beams, possessing the spatially inhomogeneous polarization states in the cross section of light, have attracted tremendous attention in optical communication[11], optical micromanipulation[12], high-numerical-aperture focusing[13], and polarization pattern

entanglement[14]. Their polarization features, such as singularities[15] and the Pancharatnam–Berry phase[16], have been widely explored. Some researchers have also investigated the SHG process of vector beams, including the vector Gaussian beam[17], the vortex beams with radial or azimuthal polarization[18,19], and the cylindrical vector beam[20]. Besides, the singularities contribution[21] and the conservation of topological charge[22] during the SHG process were investigated. Recently, we also visualized the hidden topological structures of a full Poincaré (FP) beam via type II SHG in the potassium titanyl phosphate (KTP) crystals[23]. However, we note that, due to the type II phase-matching condition, the vectorial feature of the fundamental light with spatially inhomogeneous polarization cannot be well maintained after the SHG process; namely, the generated SHG beam becomes merely a scalar light field with a uniform polarization state.

We also note that the polarization state of light usually plays an irreplaceable role in optical manipulation[24], optical communication[25], and lithography[26]. In this regard, how to maintain the vectorial nature of light fields during the process of SHG is meaningful and desirable from both the theoretical and applied points of view. Here, we present an experiment to realize SHG from infrared vector fields to visible vector fields, based on two cascading type I phase-matching beta barium borate (BBO) crystals, whose fast axes are just configured to be perpendicular to each other. It is noted that such a two-crystal geometry was actually not new[27,28], which can be traced back to the seminal work of constructing a bright source of polarization-entangled photon pairs via parametric down-conversion[29]. Here, we further explored such a configuration for an experimental

demonstration of the full vectorial feature in the SHG process, i.e., converting a fundamental wave of infrared FP beams to a visible SHG wave of FP beams. By using Stokes polarimetry, we also visualize the structured features of vectorial SHG fields and reveal the interesting doubling effect of the polarization topological index, in contrast to the invariance feature for polarization singularities of L lines and C points.

As a typical vector light field, the FP beams possess spatially varying polarization states covering the entire Poincaré sphere[30,31]. Generally, the arbitrary-order FP beams can be constructed by using a superposition of a fundamental Gaussian beam and arbitrary-order Laguerre–Gaussian (LG) beams bearing orthogonal polarizations, mathematically expressed as[23,32]

$$\boldsymbol{E}(r,\varphi) = A \cdot \mathrm{LG}_0^0(r,\varphi)\boldsymbol{e}_1 + B \cdot \mathrm{LG}_0^l(r,\varphi)\boldsymbol{e}_2 \quad (1)$$

in the cylinder coordinates, where $\boldsymbol{e}_1$ and $\boldsymbol{e}_2$ represent the unit vectors of left- and right-hand circular components, respectively, and A and B are two controllable parameters used to regulate the polarization distribution of the FP beam. The lth LG beam $\mathrm{LG}_0^l(r,\varphi)$ can be described as

$$\mathrm{LG}_0^l(r,\varphi) = E_0 r^{|l|} L_0^{|l|}\left(\frac{2r}{w^2}\right)\exp\left(-\frac{r^2}{w^2}\right)\exp(il\varphi), \quad (2)$$

where φ is the azimuthal angle, w is the beam waist, $L_0^{|l|}(\,\cdot\,)$ is the associated Laguerre polynomials, and l is an integer. In Ref. [23], we presented a stable yet flexibly controlled method to generate FP beams by the combination of the spatial light modulator (SLM), the half-wave plate (HWP), quarter-wave plate (QWP) with its fast axis orienting at 45°, and the vortex HWP (VHWP). The obtained light fields can be described as

$$\mathrm{LG}_0^0(r,\varphi)\begin{pmatrix}1\\0\end{pmatrix} \to \frac{(1+i)\cos(2\alpha)}{2}\mathrm{LG}_0^0(r,\varphi)\begin{pmatrix}1\\i\end{pmatrix}$$
$$+\frac{(1-i)\sin(2\alpha)}{2}\mathrm{LG}_0^2(r,\varphi)\begin{pmatrix}1\\-i\end{pmatrix}, \quad (3)$$

where α denotes the orientation of the fast axis of HWP, which can control the polarization distribution of FP beams. Here, we also adopt this method to generate the fundamental FP beams.

As was demonstrated in our single-crystal scheme[23], due to the phase-matching condition, SHG merely yields the scalar beams, i.e., light fields with uniform polarization distribution. From Eq. (1), one can see that the FP beams are the superposition of two orthogonal polarization components, which inspires us to construct the SHG process for each polarization component independently. Thus, we use the QWP with its fast axis orienting

at 45° to decompose the FP beam into the horizontal and the vertical components:

$$\mathrm{LG}_0^0(r,\varphi)\begin{pmatrix}1\\0\end{pmatrix} \to i\cos(2\alpha)\mathrm{LG}_0^0(r,\varphi)\begin{pmatrix}1\\0\end{pmatrix}$$
$$-i\sin(2\alpha)\mathrm{LG}_0^2(r,\varphi)\begin{pmatrix}0\\1\end{pmatrix}. \quad (4)$$

We direct these two polarization components to pass through two cascading BBO crystals, whose fast axes are just configured to be perpendicular to each other. Besides, both crystals are cut for type I phase-matching to implement the SHG process. Thus, we know that in the first BBO crystal only the horizontal polarization component in Eq. (4) participates in the process of SHG, generating a frequency-doubled light field of vertical polarization. While in the second BBO crystal, only the vertical polarization component in Eq. (4) participates in SHG, yielding a frequency-doubled light field of horizontal polarization. Under the paraxial approximation and the phase-matching condition, the process of frequency doubling in these two crystals can be described, respectively, by the following wave coupling equations:

$$\frac{\mathrm{d}E_{SH}^V}{\mathrm{d}z} = \frac{i\omega_{SH}^2 d_{\mathrm{eff}}}{k_{SH}c^2}E_H^2,$$
$$\frac{\mathrm{d}E_{SH}^H}{\mathrm{d}z} = \frac{i\omega_{SH}^2 d_{\mathrm{eff}}}{k_{SH}c^2}E_V^2, \quad (5)$$

where d_{eff} is the effective nonlinear coefficient, ω_{SH} and k_{SH} are the angular frequency and wave vector of the SHG beam, c is the velocity of light, and E_H and E_V represent the horizontal and vertical polarization fundamental light fields, respectively. Under the small-signal approximation, the SHG light fields of orthogonal polarizations can be approximately expressed as $E_{SH}^V \propto E_H^2$ and $E_{SH}^H \propto E_V^2$, respectively. After SHG, another complementary QWP with its fast axis orienting at 45° is arranged to recombine E_{SH}^V and E_{SH}^H. Accordingly, we have the output SHG beams

$$\mathrm{LG}_0^0(r,\varphi)\begin{pmatrix}1\\0\end{pmatrix} \to -\cos^2(2\alpha)[\mathrm{LG}_0^0(r,\varphi)]^2\begin{pmatrix}1\\i\end{pmatrix}$$
$$+\sin^2(2\alpha)[\mathrm{LG}_0^2(r,\varphi)]^2\begin{pmatrix}1\\-i\end{pmatrix}, \quad (6)$$

which clearly reveals the acquisition of a higher topological index, relative to that of the fundamental wave described by Eq. (3). In other words, our scheme can easily realize the frequency conversion from one FP beam to another high-order FP beam, i.e., the vectorial feature can be well preserved during the process of SHG.

We display our experimental setup in Fig. 1. After being collimated and expanded by a telescope, the horizontally polarized 1064 nm laser beams with power of 200 mW successively pass through HWP$_1$ (1064 nm), QWP$_1$ (1064 nm) with its fast axis orienting at 45°, a vortex

phase plate with unit topological charge (VPP, RPC Photonics), and VHWP (Thorlabs, WPV10 L-1064) to produce the desired fundamental FP beams by adjusting the fast-axis orientation of HWP_1 [23], see Fig. 1(a), for example. It is worth noting that the VPP here is used to generate the LG_0^1 mode. Then, QWP_2 (1064 nm) with its fast axis orienting at 45° is used to decompose the generated FP beams into two orthogonal components, e.g., the horizontal and vertical polarization, respectively.

These two components are imaged via a $4f$ imaging system ($f_1 = 750$ mm, $f_2 = 500$ mm) onto two cascading BBO crystals (8 mm × 8 mm × 2 mm), whose fast axes are set perpendicularly to each other. It was noted that we use two thin crystals such that the walk-off effect could be eliminated effectively. As a result, we implement the SHG process described by Eq. (5). After QWP_3 (532 nm), the generated SHG beams of horizontal and vertical polarizations superpose to form the desired FP beams finally, as illustrated in Fig. 1(b).

In order to exactly characterize the polarization states of SHG beams, we conduct the standard Stokes polarimetry with the following HWP_2, QWP_4, and polarizer, as shown in Fig. 1. Theoretically, the Stokes parameters can be expressed as[33,34]

$$\begin{cases} s_0 = I_H + I_V \\ s_1 = I_H - I_V \\ s_2 = I_D - I_A \\ s_3 = I_R - I_L \end{cases}, \quad (7)$$

where $I_{(\cdot)}$ represents the light intensity of the horizontal (H), vertical (V), 45° (D), 135° (A), right-hand (R) or the left-hand (L) polarization component of the SHG beam.

Accordingly, one can derive the polarization distribution of an optical field in the experiment via measuring the intensity of the aforementioned six components. For this, we arrange the fast axes of HWP_2, QWP_4, and the polarizer as shown in Table 1, where the symbol "-" denotes the unnecessary use of the optical elements. With a CCD camera (Thorlabs, DCU224 C), we can easily obtain the spatially varying polarization states point-by-point across the optical field. Here, for capturing the clear optical patterns, we use L_3 to image the generated SHG beams on the CCD camera.
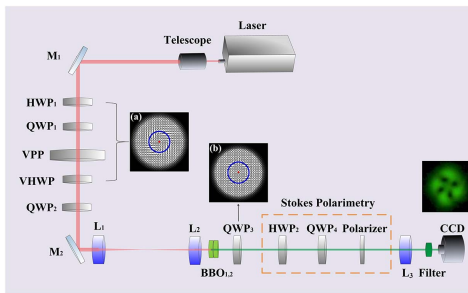

Fig. 1. Experimental setup for SHG of FP beams in BBO crystals.

Table 1. Settings of the Optical Elements in the Setup to Detect the States of Polarization

	States					
Elements	H	V	A	D	R	L
HWP_2	–	–	22.5°	22.5°	–	–
QWP_4	–	–	–	–	45°	45°
Polarizer	0°	90°	0°	90°	0°	90°

In our first set of experiments, we verify the effectiveness of Stokes polarimetry by preparing the fundamental FP beams in the cases of $\alpha = 15°$ and 30°, see Eqs. (3) and (4). After the cascading SHG process and Stokes polarimetry, the experimental observations of the six aforementioned polarization components are presented in the first rows of both Figs. 2 and 3. We can see that the four linear polarization components, H, V, A, and D, all exhibit the interference patterns between the fundamental mode and high-order mode, thus, generating four symmetrical off-axis optical vortices, all with a single topological charge, while the two circular polarization components are purely the fundamental mode for L and high-order mode for R, which conforms to the theoretical simulations shown by the second rows of both Figs. 2 and 3. According to Eq. (7), we can calculate straightforwardly the Stokes parameters, as shown in the third row. For comparison, we also present the theoretical simulations, as shown by the fourth rows of both Figs. 2 and 3, from which good agreement can be seen clearly.

To have a more institutive picture of the spatially varying polarization states, we also plot the polarization ellipse from point to point, by means of the rectifying phase $\chi = \arcsin(s_3/s_0)/2$ and the orientation angle $\psi = \arg(s_1 + is_2)/2$ of local polarization ellipses[16]. According to Eq. (7) and the experimental results of
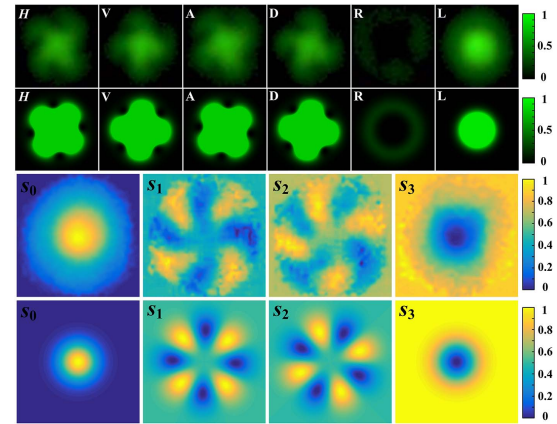

Fig. 2. Polarization and Stokes components for an output SHG light field with $\alpha = 15°$. The first and second rows show the experimental and theoretical results for the six polarization components, respectively. The third and fourth rows show the experimental and theoretical Stokes components, respectively.
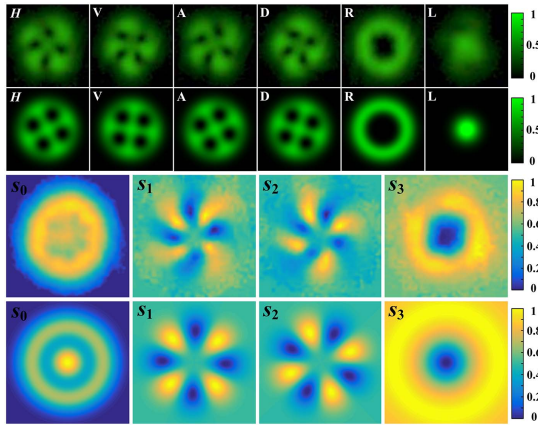
Fig. 3. Polarization and Stokes components for an output SHG light field with $\alpha = 30°$. The first and second rows show the experimental and theoretical results for the six polarization components, respectively. The third and fourth rows show the experimental and theoretical Stokes components, respectively.

Figs. 2 and 3, we calculate and visualize the polarization distributions of the SHG beams, as shown by the bottom panel of Fig. 4.

For comparison, we present the simulation results of polarization distribution for both the fundamental and SHG light waves in the top and middle panels, respectively. For the two particular cases, $\alpha = 0°$ and $\alpha = 45°$, since the fundamental beams degrade into the purely circularly polarized LG beam, the generated SHG beams are merely scalar. Of special interests are the rest cases. For both the fundamental and SHG light fields, their polarization states across the transverse plane can cover the entire surface of the Poincaré sphere. In other words, the vectorial feature of the FP beams can be well maintained in our scheme during the process of SHG. Besides, it is worth noting that the polarization distribution of fundamental beams has the "spiral" structure possessing the topological index $T = 2$, which is just equal to the topological charge of the high-order LG mode in Eq. (3). While for the generated SHG light field, the
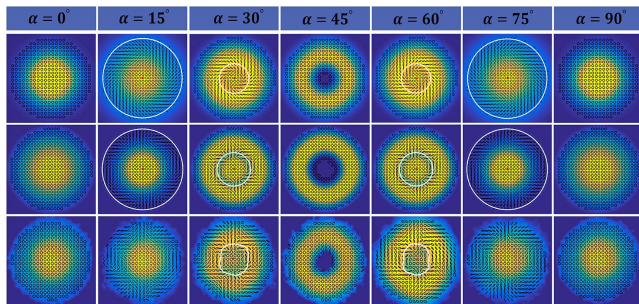

Fig. 4. Polarization distribution of SHG beams with 532 nm at $\alpha = 0°$, 15°, 30°, 45°, 60°, 75°, 90°. Top panel, numerical simulations of the polarization distribution of fundamental beams; middle panel, numerical simulations of the polarization distribution of SHG beams; bottom panel, experimental results of the polarization distribution of SHG beams.

polarization distribution of SHG beams exhibits a Daisy mode and has a topological polarization index of $T = 4$, which is twice of that of the fundamental beams. That is to say, SHG doubles not only the frequency of the light wave but also the topological polarization index, i.e., a second-order infrared FP beam can be converted to a fourth-order visible one. By comparing the middle and bottom panels, one can see that the experimental results are in good agreement with the numerical simulations.

Furthermore, to describe the polarization singularities[35–37], we recall the rectifying phase χ and the orientation angle ψ. The points with $\psi = 0$ denote where the polarization direction is undefined, called C points, while those points with $\chi = 0$ denote where the polarization handedness is undefined, called L lines. Here, the C points marked with red points and the L lines marked by white circles are plotted in Fig. 4. Both fundamental and SHG FP beams have the same C-point singularity centered at the beam axis, which remains stable as α changes. Besides, even though the polarization distribution of SHG beams is different from the fundamental beams with a "spiral" pattern, the L lines behave in a similar way to that of the fundamental wave, i.e., the L circles shrink as α is changing from 0° to 45°, while they expand as α changes from 45° to 90°. It should be emphasized that L lines in the experimental cases of 15° and 75° are located in the margin of the patterns, where the intensity is quite weak, so they cannot be plotted. Thus, another feature of the LP beam's SHG in our scheme is that regardless of the doubling of the topological charge, the polarization singularities, i.e., the C points and L lines both keep invariant during the process of SHG.

Within any transverse plane of a paraxial optical field, it is useful to characterize the smoothly varying polarization by streamlines oriented along the major axis of the polarization ellipse[35,37]. For an easy visualization, we also plot in Fig. 5 the streamlines around each C point that mathematically correspond to the theoretical and experimental results at $\alpha = 30°$, e.g., the third column of Fig. 4. For the fundamental FP beam of Fig. 5(a), the "spiral" structure of polarization states can be seen intuitively. While for the SHG FP beams, we can see that the spatially varying polarization states exhibit an interesting structure, appearing like the distribution of the electric field emitted by an electric dipole consisting of
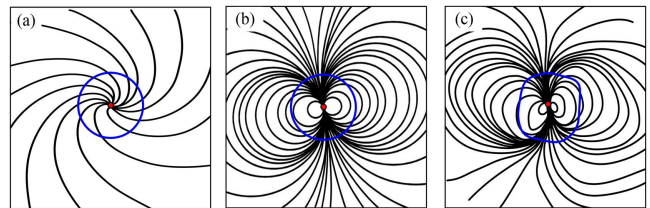

Fig. 5. Streamlines around C points at $\alpha = 30°$. (a) Numerical result for fundamental FP beam; (b) and (c) numerical and experimental results of the SHG FP beam, respectively. Blue lines and red points denote the L lines and C points, respectively.

two-point electric charges with opposite polarity. Besides, the C point in Fig. 5(b) or 5(c) can be classified by the streamlines of its immediate surroundings into two "lemons", e.g., appearing like the north and south poles, respectively.

In summary, we have realized the full vectorial SHG from infrared FP beams to visible FP beams based on two-crystal geometry. Our experimental observation reveals the interesting doubling effect of the topological index, i.e., a low-order FP beam can be effectively converted to a high-order one. Furthermore, the polarization singularities of FP beams, such as C points and L lines, both can keep invariant during SHG. This work may offer a deeper investigation on the interaction of vectorial light fields with media and find potential applications in optical imaging and material characterization.

References

1. P. A. Franken, A. E. Hill, C. W. el Peters, and G. Weinreich, Phys. Rev. Lett. **7**, 118 (1961).
2. D. A. Kleinman, Phys. Rev. Lett. **128**, 1761 (1962).
3. N. Bloembergen, R. K. Chang, S. S. Jha, and C. H. Lee, Phys. Rev. **174**, 813 (1968).
4. T. F. Heinz, C. K. Chen, D. Ricard, and Y. R. Shen, Phys. Rev. Lett. **48**, 478 (1982).
5. I. Freund, M. Deutsch, and A. Sprecher, Biophys. J. **50**, 693 (1986).
6. P. Campagnola, Anal. Chem. **83**, 3224 (2011).
7. X. Liu, D. Hua, L. Fu, and S. Zeng, Chin. Opt. Lett. **15**, 090003 (2017).
8. S. Cui, L. Zhang, H. Jiang, and Y. Feng, Chin. Opt. Lett. **15**, 041402 (2017).
9. X. Qiu, F. Li, H. Liu, X. Chen, and L. Chen, Photon. Res. **6**, 641 (2018).
10. X. Qiu, F. Li, W. Zhang, Z. Zhu, and L. Chen, Optica **5**, 208 (2018).
11. J. Wang, Photon. Res. **4**, B14 (2016).
12. L. G. Wang, Opt. Express **20**, 20814 (2012).
13. R. Dorn, S. Quabis, and G. Leuchs, Phys. Rev. Lett. **91**, 233901 (2003).
14. H. Larocque, D. Sugic, D. Mortimer, A. J. Taylor, R. Fikler, R. W. Boyd, M. R. Dennis, and E. Karimi, Nature Phys. **14**, 1079 (2018).
15. M. R. Dennis, Opt. Commun. **213**, 201 (2002).
16. G. Milione, S. Evans, D. A. Nolan, and R. R. Alfano, Phys. Rev. Lett. **108**, 190401 (2012).
17. S. Carrasco, B. E. A. Saleh, M. C. Teich, and J. Fourkas, J. Opt. Soc. Am. B **23**, 2134 (2006).
18. A. Ohtsu, Opt. Comm. **283**, 3831 (2010).
19. P. Stanislovaitis, A. Matijošius, V. Šetkus, and V. Smilgevičius, Lithuanian J. Phys. **54**, 142 (2014).
20. F. Xiao, W. Shang, W. Zhu, L. Han, M. Premaratne, T. Mei, and J. Zhao, Photon. Res. **6**, 157 (2018).
21. I. Freund, Opt. Lett. **27**, 1640 (2002).
22. P. Stanislovaitis, A. Matijosius, M. Ivanov, and V. Smilgevicius, J. Opt. **19**, 105603 (2017).
23. L. Zhang, X. Qiu, F. Li, H. Liu, X. Chen, and L. Chen, Opt. Express **26**, 11678 (2018).
24. Q. Zhan, Adv. Opt. Photon. **1**, 1 (2009).
25. Y. Han and G. Li, Opt. Express **13**, 7527 (2005).
26. M. Totzeck, W. Ulrich, A. Göhnermeier, and W. Kaiser, Nature Photon. **1**, 629 (2007).
27. L. Zhang, F. Lin, X. Qiu, and L. Chen, "Vectorial nonlinear optical generation," arXiv:1811.07102 (2018).
28. H. Liu, H. Li, Y. Zheng, and X. Chen, Opt. Lett. **43**, 5981 (2018).
29. P. G. Kwiat, E. Waks, A. G. White, I. Appelbaum, and P. H. Eberhard, Phys. Rev. A **60**, R773 (1999).
30. A. M. Beckley, T. G. Brown, and M. A. Alonso, Opt. Express **18**, 10777 (2010).
31. X. Wang, Y. Li, J. Chen, C. Guo, J. Ding, and H. Wang, Opt. Express **18**, 10786 (2010).
32. D. Naidoo, F. S. Roux, A. Dudley, I. Litvin, B. Piccirillo, L. Marrucci, and A. Forbes, Nat. Photon. **10**, 327 (2016).
33. M. R. Dennis and M. A. Alonso, Phil. Trans. Roy. Soc. A **375**, 20150441 (2017).
34. S. Chen, X. Zhou, Y. Liu, X. Ling, H. Luo, and S. Wen, Opt. Lett. **39**, 5274 (2014).
35. F. Flossmann, U. T. Schwarz, M. Maier, and M. R. Dennis, Phys. Rev. Lett. **95**, 253901 (2005).
36. F. Flossmann, K. O'Holleran, M. R. Dennis, and M. J. Padgett, Phys. Rev. Lett. **100**, 203902 (2008).
37. F. Cardano, E. Karimi, L. Marrucci, C. de Lisio, and E. Santamato, Opt. Express **21**, 8815 (2013).